Molecular structure of an N-terminal phosphorylated β-amyloid fibril

Zhi-Wen Hu[a], Liliya Vugmeyster[b,1], Dan Fai Au[b], Dmitry Ostrovsky[c], Yan Sun[d], and Wei Qiang[a,1]

[a]Department of Chemistry, Binghamton University, Binghamton, NY 13902; [b]Department of Chemistry, University of Colorado Denver, Denver, CO 80204; [c]Department of Mathematics, University of Colorado Denver, Denver, CO 80204; and [d]Health Science Core Facility, Small Scale System Integration and Packaging Center, Binghamton University, Binghamton, NY 13902

The structural polymorphism in β-amyloid (Aβ) plaques from Alzheimer disease (AD) has been recognized as an important pathological factor. Plaques from sporadic AD patients contain fibrillar deposits of various amyloid proteins/peptides, including posttranslational modified Aβ (PTM-Aβ) subtypes. Although many PTM-Aβs were shown to accelerate the fibrillation process, increase neuronal cytotoxicity of aggregates, or enhance the stability of fibrils, the contribution of PTM-Aβs to structural polymorphisms and their pathological roles remains unclear. We report here the NMR-based structure for the Ser-8-phosphorylated 40-residue Aβ (pS8-Aβ$_{40}$) fibrils, which shows significant difference to the wild-type fibrils, with higher cross-seeding efficiency and thermodynamic stability. Given these physicochemical properties, the structures originated from pS8-Aβ$_{40}$ fibrils may potentially dominate the polymorphisms in the mixture of wild-type and phosphorylated Aβ deposits. Our results imply that Aβ subtypes with "seeding-prone" properties may influence the polymorphisms of amyloid plaques through the cross-seeding process.

β-amyloid fibrils | posttranslational modification | structural polymorphism | solid-state NMR spectroscopy

Recent structural analysis of the β-amyloid (Aβ) fibrils derived from plaques from Alzheimer disease (AD) patients shed light on the pathological significance of structural polymorphisms in amyloid deposits (1). Particularly, structural polymorphisms in 40-residue Aβ (Aβ$_{40}$) fibrils were shown to correlate with clinical symptoms in different AD cases and the lengths of disease progression (1, 2). The ex vivo brain-seeded fibrillation of Aβ elucidated that fibrils were produced when seeds were extracted from AD patients, but not from non-AD controls (3, 4). Meanwhile, exogenous injection of AD brain extracts was shown to induce the formation of plaques in transgenic mice models in vivo, with the inducibility correlated with the stability, the deposition pattern, and the composition of the extracts (5–7). These findings implied that certain fibrillar structures in the pathological plaques might have higher efficiency to amplify the amyloid deposition compared to those in the nonpathological plaques. Recently, it has been shown that the amyloid deposits form conformation-distinct "clouds" that could be targeted using specific fluorescence-based molecular probes (8). It is possible that certain plaques contain fibrillar aggregates with more seeding-prone polymorphisms, and therefore could more actively induce aggregation of other amyloid species.

A fundamental question that remains unsolved is whether such seeding-prone structures originated from the wild-type (wt) Aβ peptides. Although wt-Aβ$_{40}$ and wt-Aβ$_{42}$ are the most abundant components in plaques, the answer to this question is not necessarily straightforward because the molecular structures of Aβ fibrils could propagate through cross-seeding between different amyloid proteins (9–11). Fibrillar structures originally from other amyloidosis species with seeding-prone properties may dominate the polymorphisms after long-time evolution. Several types of posttranslational modified Aβ (PTM-Aβ) fibrils have been identified in pathological amyloid plaques (12). Immuno-blotting assays showed that a few critical PTM-Aβ subtypes, including the

E3- and E11-pyroglutarmation (13, 14), the D7-isomerization (15), the S8-phosphorylation (13, 16), the S26-phosphorylation (17), and the Y10-nitration of Aβ (18), either concentrated in the plaque core or formed fibrils earlier than the wt-Aβ peptides. In vitro studies have also demonstrated that certain PTM-Aβs grew fibrils more rapidly than their wt-Aβ analogs and possessed higher levels of neuronal cytotoxicity (9, 18, 19). Certain PTM-Aβ subtypes were thought to trigger or accelerate the fibrillation of wt-Aβ peptides (20, 21). However, the structural basis of the pathological roles of PTM-Aβs has not been determined.

Results

The Molecular Structure of Ser-8-Phosphorylated Aβ$_{40}$ Fibril. We previously demonstrated that the S8-phosphorylated Aβ$_{40}$ (pS8-Aβ$_{40}$), a PTM-Aβ identified in pathological AD plaques, possessed high cross-seeding efficiencies to multiple Aβ subtypes, including the wt-Aβ$_{40}$, wt-Aβ$_{42}$, and E3-pyroglutamated Aβ$_{40}$ (22). This work reports the molecular structure of pS8-Aβ$_{40}$ fibril (Fig. 1A) and investigates its potential to dominate structural polymorphisms in a mixed fibrillar system. The pS8-Aβ$_{40}$ fibrils were grown from synthetic peptides in physiological buffer (i.e., pH 7.4 and 37 °C) with continuous gentle agitation, followed by generation seeding to ensure structural homogeneity. Structural modeling was performed using Xplor-NIH (23) with experimental constraints from solid-state NMR (ssNMR) spectroscopy

---

Significance

This work reports the molecular structure formed by a pathologically relevant posttranslational modified β-amyloid (Aβ), the Ser-8-phosphorylated Aβ$_{40}$ (pS8-Aβ$_{40}$). The N-terminal structures in pS8-Aβ$_{40}$ fibril differ significantly from all known wild-type Aβ$_{40}$ fibrils, with strong intra-strand interactions that make the N terminus associated closely with the amyloid core. The pS8-Aβ$_{40}$ fibril possesses strong cross-seeding ability to wild-type Aβ$_{40}$ monomers, while the propagated fibrillar structure shows higher thermodynamic stability and core rigidity compared to the fibrils formed by the self-nucleation of wild-type Aβ$_{40}$. Our finding may shed light on the origin of structural polymorphisms in Aβ amyloids.
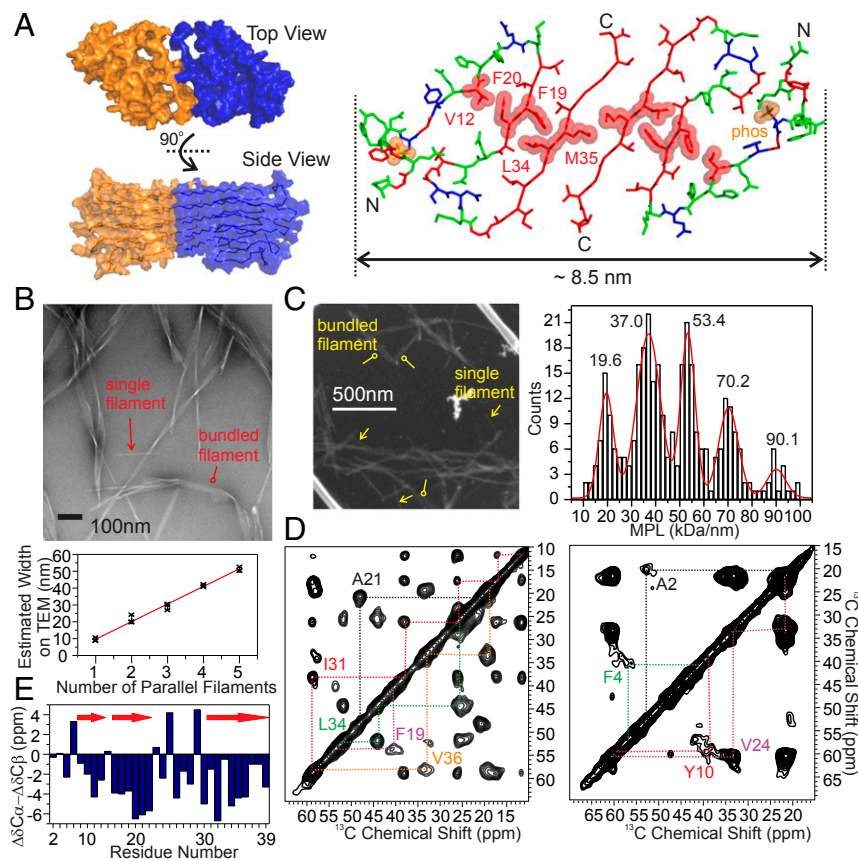

Fig. 1. The molecular structure of pS8-Aβ$_{40}$ fibrils. (A) Structural models shown in surface mode (*Left*) that highlight two subunits in orange and blue, and stick mode (*Right*) that highlights the hydrophobic, polar, and charged residues in red, blue, and green, respectively. Side chains of the residues that form key hydrophobic contacts in cores are shown in red, and the phosphate groups at S8 are shown in orange. (B, *Top*) A representative negatively stained TEM image with parallel filaments highlighted using red arrows. (B, *Bottom*) Plots of the apparent fibril widths vs. number of filaments. Error bar reflects the SD from three measurements on the fibril widths (indicated by columns) for each number of parallel filaments. (C, *Left*) A representative dark-field TEM image for the MPL measurement with single and bundled filaments highlighted using yellow arrows. (C, *Right*) The histogram plot for the analysis of MPL with Gaussian fitting. The minimum 19.5 kDa/nm corresponds to the MPL of a single twofold Aβ filament. (D) Representative 2D ssNMR spectra with lines highlighting individual intraresidue cross peaks. (E) Plots of the residue-specific differences in the secondary chemical shifts of Cα and Cβ. Negative values indicate β strand conformation (shown by red arrows on top of the bars).

and transmission electron microscopy (TEM). The fibrils showed striated-ribbon morphology similar to the twofold wt-Aβ$_{40}$ (wt2-Aβ$_{40}$) fibrils grown under similar conditions (Fig. 1B and *SI Appendix*, Fig. S1) (24, 25). The molecular structure for pS8-Aβ$_{40}$ fibrils illustrated the width ~8.5 nm across the interface perpendicular to the fibril axis, larger than the width ~6.0 nm for wt2-Aβ$_{40}$ fibrils (25). Measurements of the mass-per-length (MPL) (26) indicated that the fibrils possessed twofold symmetry (a minimum MPL ~19 kDa/nm and multiples, Fig. 1C). Three segments of β strands were identified at G9-V12, L17-E22, and I31-V39, connected by a shorter loop around H13-K16 and a longer loop around D23-A30. The N-terminal segment D1-D7 was disordered and showed broadened ssNMR peaks (Fig. 1 D and E and *SI Appendix*, Figs. S2–S4 and Table S2). Crucial long-range structural constraints were obtained using multiple types of ssNMR methods (*SI Appendix*, Figs. S5–S8 and Table S3). Interestingly, side-chain interactions between residues in G9-V12 and L17-E22 strands (Fig. 2A) were intramolecular, confirmed by 2D ^{13}C-^{13}C spin-diffusion spectroscopy with samples containing isotope-labeled and unlabeled pS8-Aβ$_{40}$ in a 1:1 molar ratio, while the interactions between L17-E22 and I31-V39 strands were intermolecular (Fig. 2B). Parallel-in-register β sheets from G9 to V39 were confirmed by ^{13}C-PITHIRDs-CT experiments (27), while A2 showed longer interstrand distance ~7.0 Å (Fig. 2C and *SI Appendix*, Fig. S9).

The pS8-Aβ$_{40}$ fibril showed distinct structural features compared to wt-Aβ fibrils (24, 25). Most strikingly, the N-terminal conformation was unique. The wt2-Aβ$_{40}$ fibrils showed highly dynamic N terminus, where residues D1-S8 were disordered and G9-Q15 were not involved in the fibrillar core (24). Disordered N-terminal segments were also reported for the threefold wt-Aβ$_{40}$ (wt3-Aβ$_{40}$) fibril, grown in vitro from synthetic peptides (25). The ex vivo brain-seeded Aβ$_{40}$ fibril possessed well-defined parallel-in-register β-sheet through the entire sequence; however, with intermolecular contacts between the N terminus of one strand and the E22-A30 loop of the adjacent

strand (4). In contrast, the pS8-Aβ$_{40}$ fibril showed strong intrastrand interactions between the N terminus and the rest of amyloid core. For instance, close proximities were detected between phosphate group of pS8 and V24-G25 (Fig. 2D), and between the side chains of E3/F4 and V24/S26 (*SI Appendix*, Figs. S5 and S6), suggesting that the N-terminal residues might participate in the initial aggregation to form protofibrils. The ^{31}P-^{31}P interstrand distance was ~6.5 Å (^{31}P-PITHIRDs-CT, Fig. 2E), meaning that pS8 did not belong to the parallel-in-register β sheets (the H-bond network started from G9). All phosphate side chains on pS8 pointed toward the amyloid core, consistent with our previous finding that the fibrillar pS8-Aβ$_{40}$ aggregates were more resistant to calf intestinal alkaline phosphatase than the monomeric peptides (22). Residues D1-D7 were clearly more dynamic than the rest of pS8-Aβ$_{40}$ sequence; however, there still existed certain intermolecular structural restraints, e.g., the methyl groups of A2 adopted ~7.0 Å interstrand distance (Fig. 2C). Furthermore, compared to the wt2-Aβ$_{40}$, the phosphorylated fibril (Fig. 2F) had hydrophobic side chain packing involving nine residues in its quaternary structural interface (i.e., I31 to V39), while the wild-type fibrils had only six residues (i.e., I31 to V36) (24, 25).

Quantitative Difference in Seeding Abilities Between pS8 and wt2-Aβ$_{40}$ Fibrils. We next specifically compare the seeding abilities of the pS8-Aβ$_{40}$ and wt2-Aβ$_{40}$ fibrils, which were grown under similar conditions. The thioflavin-T (ThT) fluorescence assay (Fig. 3A and *SI Appendix*, Fig. S10) on fibrillation showed kinetics that fit to single-exponential increases without lag phase. Little fluorescence increase was observed in the absence of seeds within the same period (i.e., ~10 h, *SI Appendix*, Fig. S11), confirming that self-nucleation from Aβ$_{40}$ monomers was eliminated under the present seeding conditions. Plot of the initial ThT build-up rates as a function of seed concentrations (Fig. 3B) concluded that the elongation rate constant for the seeded fibrillation with pS8-Aβ$_{40}$ was ~5 times higher than wt2-Aβ$_{40}$.
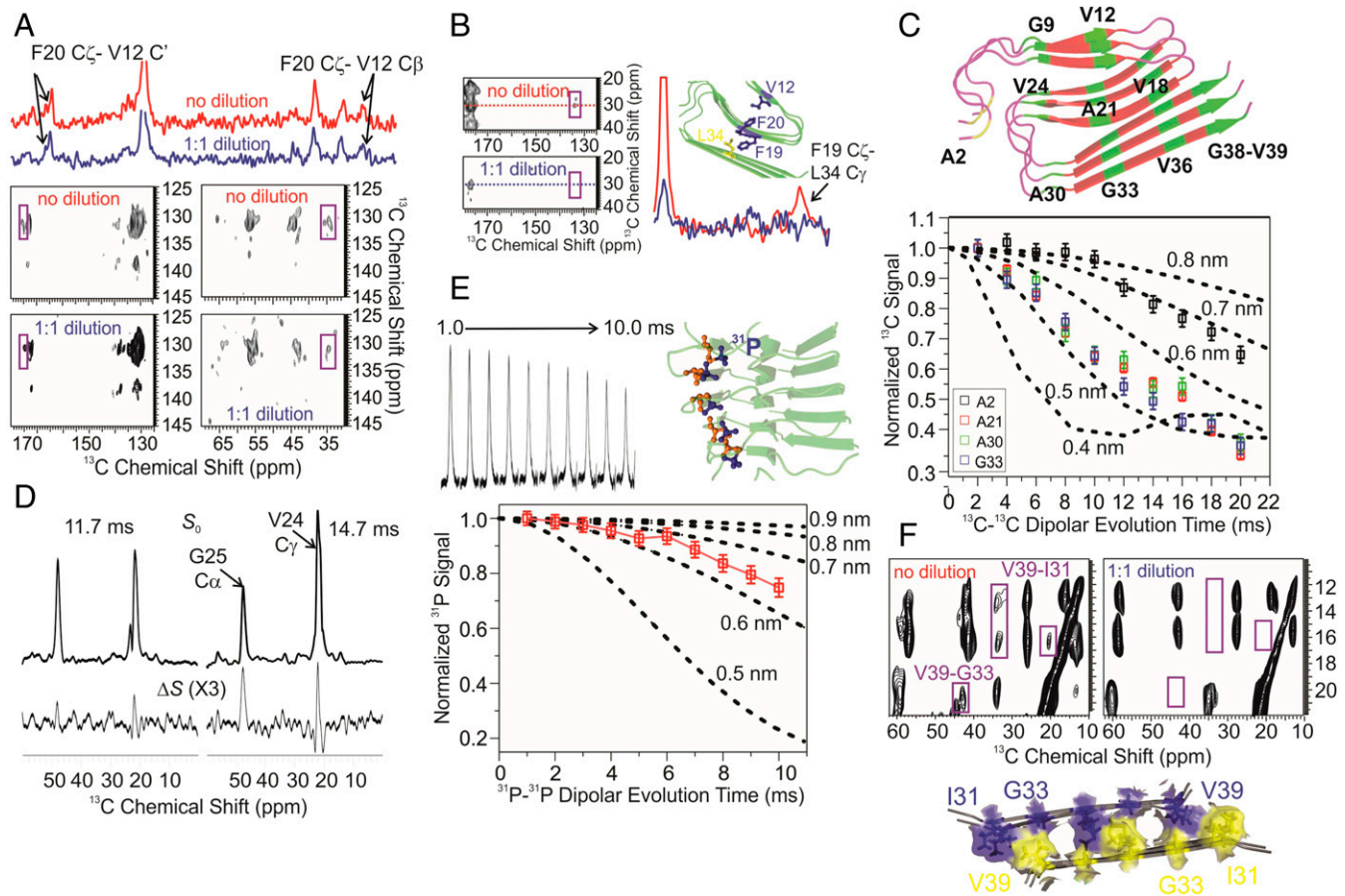
Fig. 2. Structural restraints for pS8-Aβ40 fibrils. (*A* and *B*) Representative 2D spin diffusion spectra to show interresidue cross peaks with samples that were fully isotope labeled (red, no dilution) and 50% isotope labeled (blue, 1:1 dilution). The cartoon model in *B* highlighted that the V12-F20 interaction was intrastrand (side chains shown in the same color) and the F19-L34 interaction was interstrand (side chains shown in different colors). (*C, Bottom*) Representative ¹³C-PITHIRDs-CT decay curves and simulated curves for different ¹³C-¹³C proximities. (*C, Top*) The cartoon model highlighting the full ¹³C-labeling sites for PITHIRDs measurements. Noting that A2 was not in parallel β sheet. (*D*) Representative ¹³C-³¹P REDOR original (*S₀*) and difference (Δ*S*) spectra to show the close contact between pS8 phosphate and V24/G25. (*E, Top Left*) ³¹P-PITHIRDs-CT spectra on pS8-Aβ40 fibrils. (*E, Bottom*) Plots of ³¹P dephasing and simulated ³¹P decay curves for different ³¹P-³¹P proximities. (*E, Top Right*) The cartoon model highlighting the proximities between adjacent ³¹Ps (in blue) in pS8-Aβ40 fibrils. (*F*) The 2D spin diffusion spectra on samples with and without dilution to highlight the side-chain contacts in the quaternary structural interface (*Bottom* cartoon models). In *C* and *E*, error bars reflect the spectral noise levels in corresponding PITHIRDs experiments and were obtained by integrating noises in individual spectra.

Noting that it was the wt2-Aβ40 seeds rather than the pS8-Aβ40 seeds that had the same primary sequence as monomeric peptides in the seeding system, it was clear that the seeding efficiencies were determined by molecular structures rather than the primary sequences. The ThT assays were also applied to the mixed pS8-Aβ40 and wt2-Aβ40 seeds. The results (Fig. 3 *C* and *D* and *SI Appendix*, Fig. S12) showed that with a constant total seed concentration and seed-to-monomer ratio, the initial ThT build-up rates increased linearly and the ThT emission intensities decreased linearly with the percentage of pS8-Aβ40 seeds in the mixture. These results highlighted: (*i*) the relative seeding efficiencies of pS8-Aβ40 and wt2-Aβ40 fibrils retained quantitatively in mixtures; and (*ii*) distinct morphologies of individual seeds, characterized by different levels of ThT intensities (28), were propagated to the seeded fibrils.

The pS8-Aβ40 Fibril Possesses Higher Stability and Core Rigidity. We then asked which fibril possessed higher stability, as mixed fibrillar structures with different stabilities were shown to slowly convert to the more stable one (29). Denaturing guanidine hydrochloride (GndHCl) assay (Fig. 4*A*) showed that the pS8-Aβ40 fibrils were more resistant to denaturing reagents, and therefore might possess higher thermodynamic stability. Dynamics at selected sites in amyloid cores, which indicated the core rigidity, were probed

using ²H ssNMR spectroscopy. The temperature-dependence of ²H quadrupolar line shapes and longitudinal relaxation revealed mainly the activation energies for the side chain rotameric (L17, L34, M35, and V36) and ring-flipping (F19) motions (30, 31). Our results showed the ²H line shapes for L34, M35, and V36 (Fig. 4*B*) and the ²H relaxation for F19 (Fig. 4*C*) were distinct between pS8-Aβ40 and wt2-Aβ40 fibrils. Little difference in ²H line shapes was observed for L17 (*SI Appendix*, Fig. S13). Noting that L17 was located at the edge of β sheets in both fibrils (25, 32), it seemed that these two structures had more distinct dynamic features in the center of amyloid core. Quantitative fitting of both ²H line shapes and relaxation to motional models (*SI Appendix*, Figs. S14–S17 and Tables S4–S6) led to the conclusion that the activation energies for large-scale motions, including the methyl axes rotameric jumps in L34, M35, and V36 and the ring flips in F19 (33), were larger in pS8-Aβ40 fibrils compared to wt2-Aβ40 fibrils (Fig. 4*D*), suggesting a more rigid fibrillar core for the modified fibril and in parallel with the higher thermodynamic stability in the phosphorylated fibril shown by denaturing assays.

The Presence of pS8-Aβ40 Seeds May Alter the Monomeric Aβ40 Pathway in Seeding. The combination of ThT fluorescence, GndHCl denaturing assay, and ²H NMR results led to the conclusion that the fibril structure formed by pS8-Aβ40 was more
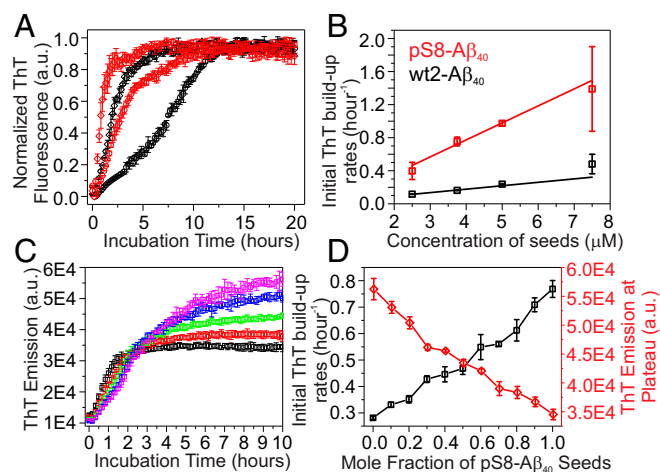
Fig. 3. ThT fluorescence kinetics assay of seeded fibrillation. (*A*) Representative ThT traces of seeded Aβ40 fibrillation with 5 mol % wt2-Aβ40 (black circles), 15 mol % wt2-Aβ40 (black diamonds), 5 mol % pS8-Aβ40 (red circles), and 15 mol % pS8-Aβ40. (*B*) Plots of the initial ThT build-up rates (extracted from single-exponential fitting of curves in A) vs. seed concentrations. The slopes indicate the elongation rate constants. (*C*) Representative ThT traces of seeded Ab40 fibrillation with mixed wt2-Aβ40 and pS8-Aβ40 seeds. The mole fraction of pS8-Aβ40 seeds were 1.0, 0.8, 0.5, 0.2, and 0.0 for curves in black, red, green, blue, and purple, respectively. (*D*) Plots of the initial ThT build-up rates (black, left vertical axis) and ThT emission at plateau (red, right vertical axis) vs. the mole fraction of pS8-Aβ40 seeds. Error bars in *A* and *C* were drawn from five independent measurements for each condition. Error bars in *B* and *D* were derived from fitting of independent corresponding ThT kinetic traces, respectively.

seeding-prone compared to wt2-Aβ40 because it induced more rapid cross-seeding to wt-Aβ40 peptides and the propagated structures possessed higher stability and rigidity. Thus, the structure propagated from pS8-Aβ40 seeds would dominate the polymorphism in Aβ deposits over time if only these two types of seeds existed, although the pS8-Aβ40 might not be the predominant species. Molecular structures of pS8-Aβ40 and wt2-Aβ40 fibrils had the most significant difference at their N termini (25, 32). We showed using the tyrosine fluorescence-quenching assay that the presence of these different seeds potentially altered the folding pathway of N termini of wt-Aβ peptides. Quenching of the Y10 side chain fluorescence with water-soluble acrylamide was sensitive to its local environment (Fig. 5*A*) (34), and therefore the slopes of quenching showed measurable differences between wt-Aβ40 peptides, wt2-Aβ40 fibrils, and pS8-Aβ40 fibrils. We then monitored the time-dependence of fluorescence quenching slopes in systems that contained the same concentration of wt-Aβ40 monomers with 10 mol % either wt2-Aβ40 or pS8-Aβ40 seeds. As shown in Fig. 5 *B* and *C*, the slopes decreased from the characteristic values for wt-Aβ monomers to the values for fibrils in both cases in the time course of fibrillation (monitored using ThT assay under the same seeding condition). Interestingly, the time dependence of quenching slopes matched qualitatively the kinetics of seeded fibrillation; i.e., the Y10 side chain folded into a water-shielded conformation more rapidly in the presence of pS8-Aβ40 seeds. Results from the fluorescence-quenching assay suggested that the more structurally ordered N terminus in pS8-Aβ40 fibril would enhance its seeding efficiency by accelerating the formation of well-ordered N termini in the "docked" monomers.

Discussion

The molecular structure of pS8-Aβ40 fibril and its seeding-prone feature have the following implications: First, the molecular architectures of Aβ pathological plaques, and the underlying fibrillar structures, may be different among specific AD subtypes (1), and different molecular strains of Aβ may propagate their features in brains (8). Here, we showed an example of how certain

fibrillar structures initiated from less abundant Aβ species might dominate the polymorphisms in amyloid deposits. If a particular amyloid plaque contains the mixture of pS8-Aβ40 and wt2-Aβ40 fibrils, and both fibrils are potential pools of seeds to induce further amyloid deposition, it is clear from our results that the structure originated from pS8-Aβ40 will become dominant after long evolution. We showed previously the pS8-Aβ40 could cross-seed not only wt-Aβ40, but also wt-Aβ42 and pyroglutamate-E3-Aβ40 (23); meaning, that the molecular structure originated from pS8-Aβ40 may propagate to multiple Aβ subtypes, which potentially enhance its dominancy in plaques. Given the highly heterogeneous compositions in pathological AD plaques and the cross-seeding nature of amyloid proteins, it is reasonable to suspect that a dominant Aβ fibril structure extracted from postmortem plaques might be originated from less-abundant morphologies (either a structure formed by a sparse amyloid species or a rare structure formed by the abundant wt-Aβ40 or wt-Aβ42), as long as such morphologies are seeding-prone. Our results on the pS8-Aβ40 suggested that this PTM-Aβ subtype could be a potential source for such seeding-prone morphology. Since other PTM-Aβ subtypes, especially the E3-pyroglutarmated Aβ, also introduce modifications to the N terminus, they may influence the seeding properties of resultant fibrillar morphologies similarly (9).

Second, our results from current and previous works (23) suggest that the quantities of certain Aβ species do not necessarily correlate with their neuronal cellular toxicities. We have shown previously that the pS8-Aβ40 fibrils possessed a higher level of cellular toxicity compared to the wt2-Aβ40 fibrils, and such difference in cytotoxicity was retained in the wt-Aβ40 fibrils grown from these two seeds (22). Therefore, for two Aβ plaques that contain both morphologies from pS8-Aβ40 and wt2-Aβ40, their relative cytotoxicity should in principle correlate with the population of the morphology that has been propagated from the original pS8-Aβ40 fibril structures, rather than the absolute quantities of either wt-Aβ40 or pS8-Aβ40 peptides. Therefore, it may be critical to utilize structure-specific molecular probes (8, 35) and imaging techniques to quantify pathological AD plaques to illustrate their potential correlation with the disease progression.

Third, the molecular structure of pS8-Aβ40 fibril highlighted the significance of N terminus in manipulating both the fibrils structures and the aggregation processes. The presence of an ordered N-terminal segment in Aβ fibril structures may be biologically relevant, because most recent structural studies on the ex vivo brain-extracted Aβ40 fibrils (4) and more pathological Aβ42 fibrils (36–38) both yielded models with ordered N termini. Interestingly, a recent molecular structural model for Aβ42 fibril showed that its N terminus formed intramolecular interactions with C-terminal loop segments, similar to the present pS8-Aβ40 fibril structure. The difference was that intermolecular interactions served as the main restraints for the association between N termini and fibrillar core in those structures, while intramolecular interactions play the key role in pS8-Aβ40 fibrils. This structural feature suggests that the nucleus formed by pS8-Aβ40 fibril may contain a more structurally ordered N terminus compared to the wild-type fibrils. Elongation from such a well-ordered nucleus leads to a more stable and rigid fibrillar structure, which was proved by the denaturing assay and 2H NMR spectroscopy (Fig. 4), and further consistent with the observation that the fibrillar morphologies of pS8-Aβ40 did not vary significantly upon generation seeding (*SI Appendix*, Fig. S1). Several PTM-Aβ subtypes with modified N termini were shown to possess accelerated fibrillation kinetics and/or more stable fibril structures (9, 12, 18, 19, 39, 40). It will be worth investigating whether the presence of more ordered structures at the N termini is a common feature for PTM-Aβ fibrils and how it would correlate with the changes in the physicochemical properties of fibrillation.

Materials and Methods

Peptide Synthesis and Purification. All peptides (with different selectively labeling schemes summarized in *SI Appendix*, Table S1) were synthesized manually using routine solid-phase peptide synthesis protocols. The experimental details were provided in *SI Appendix*.
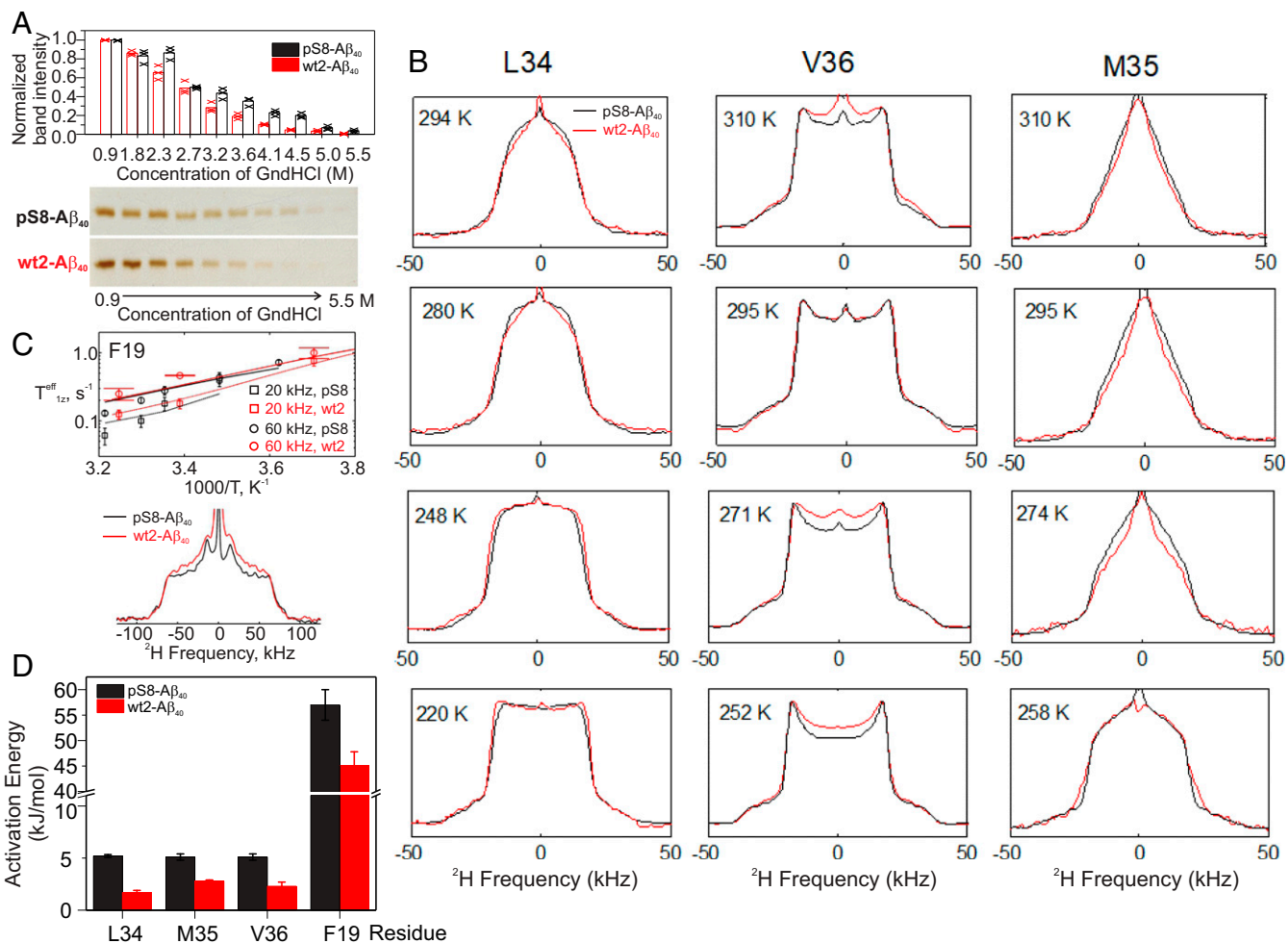
Fig. 4. Stabilities of wt2-Aβ$_{40}$ and pS8-Aβ$_{40}$ fibrils. (*A*) Denaturing gel electrophoresis assay (*Bottom*, representative gel bands) to determine the stability of pS8-Aβ$_{40}$ (*Top*, black columns) and wt2-Aβ$_{40}$ (*Top*, red columns) fibrils. The average normalized intensities (shown in columns) were obtained from three independent repeats (in cross symbols). (*B*) Experimental ^{2}H NMR static line shapes for L34 (*Left*), V36 (*Middle*), and M35 (*Right*) in the wt2-Aβ$_{40}$ (red) and pS8-Aβ$_{40}$ (black) fibrils. (*C, Top*) ^{2}H relaxation times T_{1Z}^{eff} vs. 1000/T on semilog scale obtained for ±20 kHz (squares) and ±60 kHz (circles) positions of the powder patterns for the F19 ring in wt2-Aβ$_{40}$ (red) and pS8-Aβ$_{40}$ (black) fibrils. (*C, Bottom*) ^{2}H quadrupolar echo line shapes at 310 K for the two fibrils. (*D*) Activation energies for the large-scale motions (rotameric jumps for methyl groups and ring flips for aromatic groups) in pS8-Aβ$_{40}$ (black) and wt2-Aβ$_{40}$ (red) fibrils. Error bars in *C* and *D* are SEs of data fitting to *SI Appendix*, Eq. S1 and the Arrhenius Equation, respectively.

Fibrillation. The pS8-Aβ$_{40}$ fibrils used in the present work were grown from generation seeding protocols to ensure homogeneous structure (25). The details were provided in *SI Appendix*. The twofold wt-Aβ$_{40}$ (wt2-Aβ$_{40}$) fibrils were prepared using literature protocols (24), and featured morphologies (i.e., striated ribbon) were confirmed using negatively stained TEM.

TEM. Negatively stained TEM was utilized to observe the morphology of fibrils. Briefly, a 10 μL aliquot of fibril solution was placed on a glow-discharged carbon film, supported by lacey carbon on a copper TEM grid

(300 mesh; Ted Pella Inc.) and adsorbed for 2 min. The grid was blotted, rinsed with 10 mL of deionized water, blotted, rinsed again, blotted, then stained with 2% uranyl acetate for 30 s, blotted, and dried in air. TEM images were recorded on a FEI Morgagni microscope, operating at 80 kV, equipped with a side-mounted Advantage HR camera (Advanced Microscopy Techniques). Images were recorded with 44,000× to 89,000× magnifications. Dark-field TEM images of an unstained grid were recorded for MPL measurements, as previously described (26). To analyze the MPL, integrations of intensities were measured for selected regions in fibrils, the internal

Fig. 5. Tyrosine fluorescence quenching assay on seeded Aβ$_{40}$ fibrillation. (*A*) Fluorescence quenching vs. acrylamide concentrations for Aβ$_{40}$ monomers (black), wt2-Aβ$_{40}$ fibrils (red), and pS8-Aβ$_{40}$ fibrils (blue). (*B* and *C*) Plots of fluorescence quenching slopes (purple, obtained from linear fitting in *A*, right vertical axes in both panels) vs. fibrillation time for pS8-Aβ$_{40}$ (*B*) and wt2-Aβ$_{40}$ (*C*) seeded fibrillation. Increments of ThT fluorescence within the same time scale were also shown in the same plot (blue and red, left vertical axes in both panels). Error bars in *A* indicates three independent measurements on Tyr10 fluorescence intensities under each condition. Error bars in *B* and *C* were obtained through linear fitting of individual data sets from *A*.
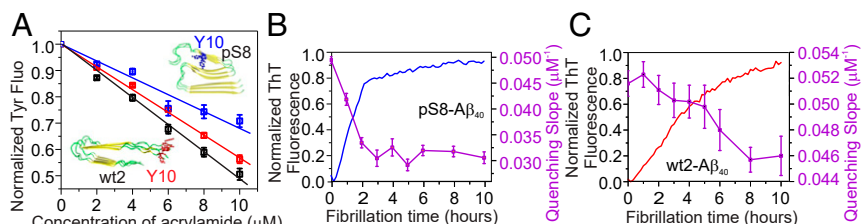
standard Tobacco Mosaic Virus (TMV), and the background of TEM grid. For the pS8-Aβ40 fibrils, which showed high tendency to form aggregated bundles, the segments with clearly separated filaments (with both single and parallel straited-ribbon filaments) were carefully selected for analysis. Over 500 segments on fibrils were analyzed from ~70 dark-field TEM images to generate the histograms shown in Fig. 1C, where individual MPL value was calculated using the equation: $MPL = (I_{TMV} - I_{B,TMV})/(I_{Fibril} - I_{B,Fibril}) \times 131 kDa/nm$, where I_{TMV} and I_{Fibril} were integrated intensities in defined areas on TMV and fibrils, and $I_{B,TMV}$ and $I_{B,Fibril}$ were integrated intensities for the size of areas of background adjacent to the selected TMV and fibrils respectively.

Thioflavin-T (ThT) Fluorescence Kinetics. The kinetics of seeded wt-Aβ40 fibrillation in the presence of the pS8-Aβ40 seeds, the wt2-Aβ40 seeds (Fig. 3A), and mixtures of pS8-Aβ40/wt2-Aβ40 seeds (Fig. 3C) were recorded by ThT fluorescence assay on a multimode plate reader (BioTek Inc.). Monomeric pS8-Aβ40/wt-Aβ40 and parent fibrils (both wt2 and pS8, 50 μM) were prepared using the protocols introduced in the previous section, and seeds were generated by sonicating the parent fibrils continuously for 30 s on ice-bath. Different volumes of seeds, monomeric wt-Aβ40 and ThT stock solution were mixed, and the final concentrations of wt-Aβ40 and ThT were 50 μM and 25 μM, respectively. Kinetics were recorded using a 96-well plate (Corning Inc.) incubated quiescently at 37 °C. Each well contains 100 μL mixed solution of fibrils and ThT stock. ThT fluorescence emission was recorded every 10 min with 10 s slow orbital shaking right before reading. Excitation and emission wavelengths were set to 450 ± 25 nm and 500 ± 13 nm, respectively, using filter sets. Three to five parallel experiments were performed for each seeded fibrillation system. Repetitions of ThT fluorescence traces were shown in *SI Appendix*, Figs. S10 and S12. Representative averaged fluorescence traces for pS8-Aβ40, wt2-Aβ40, and mixture-seeded fibrillation were reported in Fig. 3 A and C.

Thermostability Test of Fibrils Using SDS/PAGE. A 100 μL aliquot of pS8-Aβ40 or wt2-Aβ40 parent fibrils was mixed with 1 mL guanidine hydrochloride (GdnHCl) with various concentrations from 1 M to 6 M. The final concentrations of GdnHCl were from ~0.9 M to ~5.5 M, as shown in Fig. 4A. The detailed procedure was provided in *SI Appendix*.

Solid-State NMR Spectroscopy. Static ^{2}H solid-state NMR spectroscopy and ^{13}C and ^{31}P Magic Angle Spinning (MAS) solid-state NMR spectroscopy were applied to determine the core rigidity and structure of pS8-Aβ40 fibrils, respectively. Details on NMR sample preparations, data acquisition, spectral modeling, and structural modeling (using Xplor-NIH package) are included in *SI Appendix*.

Supplementary Materials Coordinates from structural modeling have been deposited into the Protein Data Bank (PDB ID 6OC9) and the assigned chemical shifts have been deposited in the Biological Magnetic Resonance Data Bank (BMRB ID 30596). Detailed descriptions of experimental procedures, including peptide synthesis, ssNMR spectroscopy and structural modeling, are provided in *SI Appendix*. Additional TEM images, ssNMR spectra, ThT kinetic traces, 2H relaxation data, as well as tables that summarizes the labeling schemes, chemical shifts, structural restraints, and fitting parameters from dynamic measurements, are also included.

1. Qiang W, Yau WM, Lu JX, Collinge J, Tycko R (2017) Structural variation in amyloid-β fibrils from Alzheimer's disease clinical subtypes. *Nature* 541:217–221.
2. Tycko R (2015) Amyloid polymorphism: Structural basis and neurobiological relevance. *Neuron* 86:632–645.
3. Paravastu AK, Qahwash I, Leapman RD, Meredith SC, Tycko R (2009) Seeded growth of beta-amyloid fibrils from Alzheimer's disease brain-derived fibrils produces a distinct fibril structure. *Proc Natl Acad Sci USA* 106:7443–7448.
4. Lu JX, et al. (2013) Molecular structure of β-amyloid fibrils in Alzheimer's disease brain tissue. *Cell* 154:1257–1268.
5. Meyer-Luehmann M, et al. (2006) Exogenous induction of cerebral β-amyloidogenesis is governed by agent and host. *Science* 313:1781–1784.
6. Watts JC, et al. (2014) Serial propagation of distinct strains of Aβ prions from Alzheimer's disease patients. *Proc Natl Acad Sci USA* 111:10323–10328.
7. Jucker M, Walker LC (2013) Self-propagation of pathogenic protein aggregates in neurodegenerative diseases. *Nature* 501:45–51.
8. Rasmussen J, et al. (2017) Amyloid polymorphisms constitute distinct clouds of conformational variants in different etiological subtypes of Alzheimer's disease. *Proc Natl Acad Sci USA* 114:13018–13023.
9. Nussbaum JM, et al. (2012) Prion-like behaviour and tau-dependent cytotoxicity of pyroglutamylated amyloid-β. *Nature* 485:651–655.
10. Horvath I, Wittung-Stafshede P (2016) Cross-talk between amyloidogenic proteins in type-2 diabetes and Parkinson's disease. *Proc Natl Acad Sci USA* 113:12473–12477.
11. He Z, et al. (2018) Amyloid-β plaques enhance Alzheimer's brain tau-seeded pathologies by facilitating neuritic plaque tau aggregation. *Nat Med* 24:29–38.
12. Kummer MP, Heneka MT (2014) Truncated and modified amyloid-β species. *Alzheimers Res Ther* 6:28.
13. Rijal Upadhaya A, et al. (2014) Biochemical stages of amyloid-β peptide aggregation and accumulation in the human brain and their association with symptomatic and pathologically preclinical Alzheimer's disease. *Brain* 137:887–903.
14. Perez-Garmendia R, et al. (2010) Anti-11[E]-pyroglutamate-modified amyloid β antibodies cross-react with other pathological Aβ species: Relevance for immunotherapy. *J Neuroimmunol* 229:248–255.
15. Moro ML, et al. (2018) Pyroglutamate and isoaspartate modified amyloid-β in ageing and Alzheimer's disease. *Acta Neuropathol Commun* 6:3.
16. Kumar S, et al. (2013) Early intraneuronal accumulation and increased aggregation of phosphorylated Abeta in a mouse model of Alzheimer's disease. *Acta Neuropathol* 125:699–709.
17. Kumar S, et al. (2016) Phosphorylation of the amyloid β-peptide at Ser26 stabilizes oligomeric assembly and increases neurotoxicity. *Acta Neuropathol* 131:525–537.
18. Kummer MP, et al. (2011) Nitration of tyrosine 10 critically enhances amyloid β aggregation and plaque formation. *Neuron* 71:833–844.
19. Kumar S, Walter J (2011) Phosphorylation of amyloid beta (Aβ) peptides–A trigger for formation of toxic aggregates in Alzheimer's disease. *Aging (Albany NY)* 3:803–812.
20. Thal DR, Walter J, Saido TC, Fändrich M (2015) Neuropathology and biochemistry of Aβ and its aggregates in Alzheimer's disease. *Acta Neuropathol* 129:167–182.
21. Barykin EP, Mitkevich VA, Kozin SA, Makarov AA (2017) Amyloid β modification: A key to the sporadic Alzheimer's disease? *Front Genet* 8:58.
22. Hu ZW, et al. (2017) Phosphorylation at Ser(8) as an intrinsic regulatory switch to regulate the morphologies and structures of Alzheimer's 40-residue beta-amyloid (A beta 40) fibrils. *J Biol Chem* 292:2611–2623, and erratum (2017) 292:8846.
23. Schwieters CD, Kuszewski JJ, Tjandra N, Clore GM (2003) The Xplor-NIH NMR molecular structure determination package. *J Magn Reson* 160:65–73.
24. Petkova AT, Yau WM, Tycko R (2006) Experimental constraints on quaternary structure in Alzheimer's β-amyloid fibrils. *Biochemistry* 45:498–512.
25. Paravastu AK, Leapman RD, Yau WM, Tycko R (2008) Molecular structural basis for polymorphism in Alzheimer's β-amyloid fibrils. *Proc Natl Acad Sci USA* 105:18349–18354.
26. Chen B, Thurber KR, Shewmaker F, Wickner RB, Tycko R (2009) Measurement of amyloid fibril mass-per-length by tilted-beam transmission electron microscopy. *Proc Natl Acad Sci USA* 106:14339–14344.
27. Tycko R (2007) Symmetry-based constant-time homonuclear dipolar recoupling in solid state NMR. *J Chem Phys* 126:064506.
28. Qiang W, Yau WM, Tycko R (2011) Structural evolution of Iowa mutant β-amyloid fibrils from polymorphic to homogeneous states under repeated seeded growth. *J Am Chem Soc* 133:4018–4029.
29. Qiang W, Kelley K, Tycko R (2013) Polymorph-specific kinetics and thermodynamics of β-amyloid fibril growth. *J Am Chem Soc* 135:6860–6871.
30. Vugmeyster LOD, Hoatson GL, Qiang W, Falconer BI (2017) Solvent-driven dynamical crossover in the phenylalanine side-chain from the hydrophobic core of amyloid fibrils detected by ^{2}H NMR relaxation. *J Phys Chem B* 121:7267–7275.
31. Vugmeyster L, et al. (2016) Fast motions of key methyl groups in amyloid-beta fibirls. *Biophys J* 111:2135–2148.
32. Tycko R (2006) Molecular structure of amyloid and prion fibrils: Insights from solid state NMR. *Nanomedicine* 2:271.
33. Vugmeyster L, et al. (2016) Flexibility and solvation of amyloid-beta hydrophobic core. *J Biol Chem* 291:18484–18495.
34. Aran Terol P, Kumita JR, Hook SC, Dobson CM, Esbjörner EK (2015) Solvent exposure of Tyr10 as a probe of structural differences between monomeric and aggregated forms of the amyloid-β peptide. *Biochem Biophys Res Commun* 468:696–701.
35. Perchiacca JML, Ladiwala AR, Bhattacharya M, Tessier PM (2012) Structure-based design of conformation- and sequence-specific antibodies against amyloid β. *Proc Natl Acad Sci USA* 109:84–89.
36. Gremer L, et al. (2017) Fibril structure of amyloid-β(1-42) by cryo-electron microscopy. *Science* 358:116–119.
37. Colvin MT, et al. (2016) Atomic resolution structure of monomorphic Aβ42 amyloid fibrils. *J Am Chem Soc* 138:9663–9674.
38. Wälti MA, et al. (2016) Atomic-resolution structure of a disease-relevant Aβ(1-42) amyloid fibril. *Proc Natl Acad Sci USA* 113:E4976–E4984.
39. Kumar S, et al. (2011) Extracellular phosphorylation of the amyloid β-peptide promotes formation of toxic aggregates during the pathogenesis of Alzheimer's disease. *EMBO J* 30:2255–2265.
40. Rezaei-Ghaleh N, Amininasab M, Kumar S, Walter J, Zweckstetter M (2016) Phosphorylation modifies the molecular stability of β-amyloid deposits. *Nat Commun* 7: 11359.